



OPEN

Cavity-enhanced field-resolved spectroscopy

Philipp Sulzer^{1,2,3,4,8}✉, Maximilian Högner^{1,2,8}✉, Ann-Kathrin Raab^{1,2,5}, Lukas Fürst^{2,6}, Ernst Fill¹, Daniel Gerz^{1,2,7}, Christina Hofer^{1,2}, Liudmila Voronina^{1,2} and Ioachim Pupeza^{1,2}✉

Femtosecond enhancement cavities¹ are key to applications including high-sensitivity linear^{2–4} and nonlinear^{5,6} gas spectroscopy, as well as efficient nonlinear optical frequency conversion^{7–10}. Yet, to date, the broadest simultaneously enhanced bandwidths amount to <20% of the central optical frequency^{8,9,11–15}. Here, we present an ultrabroadband femtosecond enhancement cavity comprising gold-coated mirrors and a wedged-diamond-plate input coupler, with an average finesse of 55 for optical frequencies below 40 THz and exceeding 40 in the 120–300 THz range. Resonant enhancement of a 50-MHz-repetition-rate offset-free frequency comb spanning 22–40 THz results in a waveform-stable ultrashort circulating pulse with a spectrum supporting a Fourier limit of 1.6 cycles, enabling time-domain electric-field-resolved spectroscopy of molecular samples with temporally separated excitation and molecular response¹⁶. The contrast between the two is improved by taking advantage of destructive interference at the input coupler. At an effective interaction length with a gas of up to 81 m, this concept promises parts-per-trillion-level ultrabroadband electric-field-resolved linear and nonlinear spectroscopy of impulsively excited molecular vibrations.

The spatial confinement of laser light propagating within passive free-space optical resonators enables multiple interactions of the circulating radiation with atoms, molecules or clusters located in the beam path. This underlies sensitivity enhancement² in techniques like cavity-enhanced absorption spectroscopy^{3,13}, cavity-ringdown spectroscopy^{4,11,12}, noise-immune cavity-enhanced optical heterodyne molecular spectroscopy¹⁷ and cavity-enhanced Vernier spectroscopy¹⁸. The same principle enables driving (extreme) nonlinear processes, like high-harmonic generation, at multi-megahertz pulse repetition rates, generating broadband frequency combs in the vacuum/extreme ultraviolet^{7–10}.

Broadband passive enhancement in a femtosecond enhancement cavity (fsEC), however, imposes challenging requirements for the mirrors, namely, simultaneous broadband reflectivity and flat spectral phase¹⁰. Consequently, typical fsECs in the ultraviolet¹², visible^{14,19} and infrared^{8,9,11,13,15,20–22} (IR) spectral regions rarely simultaneously enhance comb bandwidths broader than 10% of the central frequency, with a record value of less than 20% demonstrated in the near-IR region¹⁵. Furthermore, fsECs have so far been exclusively used in combination with time-integrating detection techniques (such as Fourier-transform infrared (FTIR) spectroscopy), requiring the detection of weak sample responses on top of—often orders of magnitude stronger—excitation intensities. This challenge to the dynamic range of linear detection^{11,20} becomes particularly severe with the advent of novel, (multi)-Watt-level mid-IR frequency combs²³.

In this Letter, we introduce ultrabroadband cavity-enhanced field-resolved spectroscopy, combining two cutting-edge photonic technologies to overcome both aforementioned shortcomings. First, employing gold-coated mirrors and reflective input coupling via a wedged^{24,25} diamond plate oriented close to Brewster's angle, we realized an fsEC with a finesse exceeding 40 over multiple octaves, and demonstrated the simultaneous enhancement of an offset-free frequency comb in the 22–40 THz range. Second, the pulse-to-pulse carrier-envelope-phase (CEP)-stable electric field of this offset-free comb enables time-domain optical-waveform detection via free-space electro-optic sampling (EOS)^{26,27}. This leverages the unparalleled dynamic range of linear detection and the excitation-power scalability afforded by EOS in the molecular fingerprint region^{16,28}. The combination of fsEC, impulsive excitation and EOS possesses the additional advantages of temporal separation of the resonantly enhanced sample-specific molecular response from the few-cycle excitation¹⁶ and the potentially strong attenuation of the few-cycle excitation owing to destructive interference at the input coupler (IC).

The working principle of an fsEC resonantly seeded by a train of CEP-stable pulses (red) is illustrated in Fig. 1a. Provided the comb lines of the driving laser overlap with the fsEC's resonances, the seeding and circulating pulses constructively interfere inside the cavity, whereas the immediate reflection of the seeding pulses off the IC interferes destructively with a portion of the circulating field transmitted through the IC. In the case of a perfectly impedance- and mode-matched fsEC, this leads to a complete suppression of the reflected field. This changes, however, when a gas with optically active molecular vibrations is introduced in the beam path. The coherent electric field emitted as a consequence of the impulsive vibrational excitation (that is, the molecular response) consists of long-lasting oscillations (green), which, after excitation, lack a matching counterpart to destructively interfere with at the IC. Consequently, the beam reflected off the fsEC contains the enhanced molecular response and suppresses the excitation pulse.

The field-resolved spectroscopy setup, which we used to elucidate these phenomena in the time domain, is sketched in Fig. 1b. A fibre-laser front end generates a frequency comb with controllable repetition rate f_{rep} and offset frequency f_0 (Methods). Intrapulse difference-frequency generation (IPDFG) in a 1-mm-thick GaSe crystal inherently generates an offset-free frequency comb with an average power of approximately 0.1 W, which then seeds the fsEC. Figure 1c depicts the fsEC design. Reflective input/output coupling by means of a wedged diamond obviates the need of a partially transmissive input coupling mirror, enabling the exclusive

¹Max-Planck-Institut für Quantenoptik, Garching, Germany. ²Ludwig-Maximilians-Universität München, Garching, Germany. ³Department of Physics and Astronomy, University of British Columbia, Vancouver, British Columbia, Canada. ⁴Quantum Matter Institute, University of British Columbia, Vancouver, British Columbia, Canada. ⁵Department of Physics, Lund University, Lund, Sweden. ⁶Institute of Experimental Physics, Graz University of Technology, Graz, Austria. ⁷Leibniz Institute of Photonic Technology—Member of the Research Alliance 'Leibniz Health Technologies', Jena, Germany. ⁸These authors contributed equally: Philipp Sulzer, Maximilian Högner. ✉e-mail: philipp.sulzer@ubc.ca; maximilian.hoegner@mpq.mpg.de; ioachim.pupeza@mpq.mpg.de

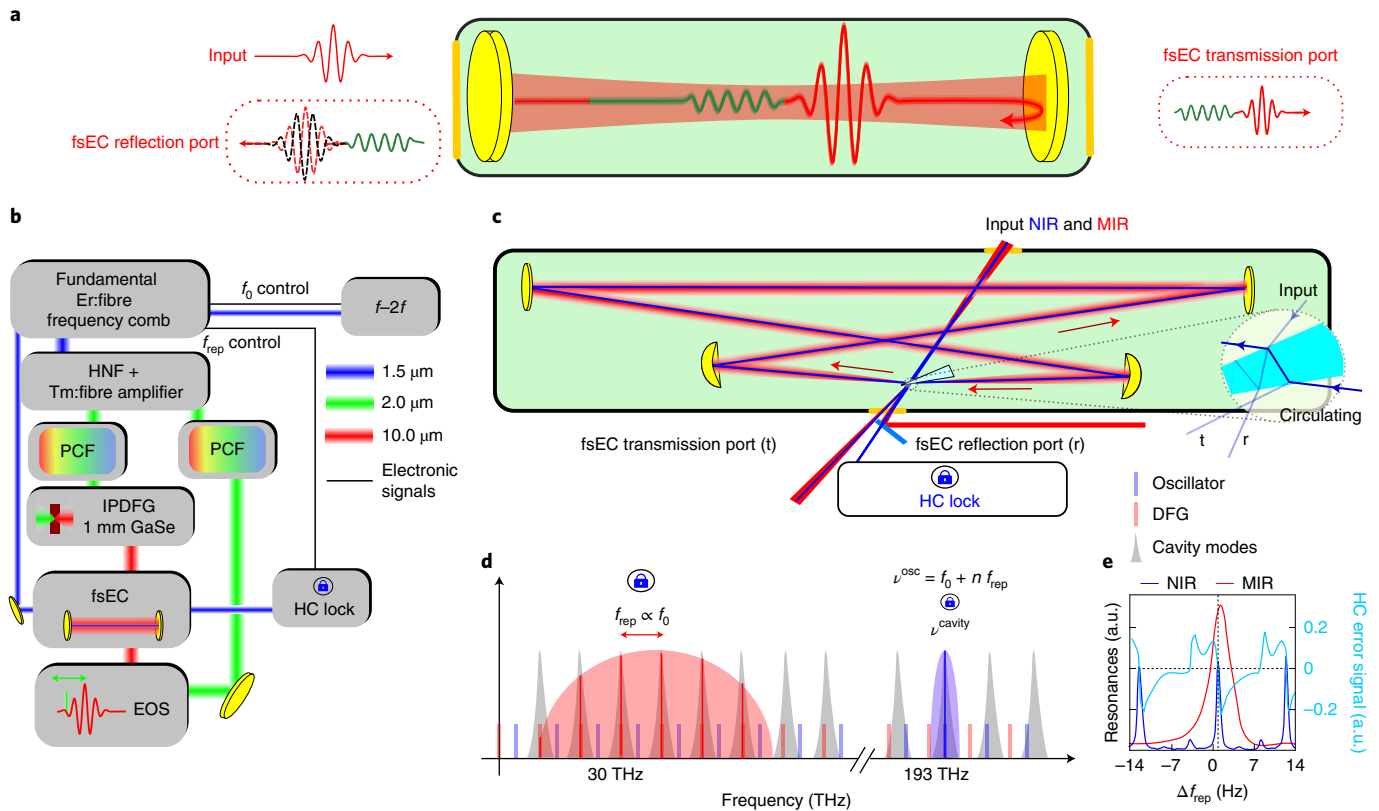


Fig. 1 | Concepts and experimental implementation. **a**, Principle of the time-resolved response of an impedance-matched passive fsEC to a seeding train of ultrashort pulses. The fsEC is placed in a chamber containing molecules with IR-active vibrations. Red, exciting pulses; green, re-emitted electric field (molecular signal); black (dashed), IC reflection. **b**, Experimental setup with the fundamental frequency comb (blue) generated by an Er:fibre oscillator with nonlinear frequency conversion in a highly nonlinear fibre (HNF) and Tm:fibre-based chirped-pulse amplification (green) followed by nonlinear pulse compression in a photonic crystal fibre (PCF). IPDFG in a 1-mm-thick GaSe crystal generates an offset-free frequency comb in the mid-IR spectral region (red), which seeds the fsEC. Additional seeding with the fundamental near-IR (NIR) comb enables the generation of a Hänsch-Couillaud (HC) error signal in the near-IR region (Methods). EOS analyses the fsEC output. $f-2f$ interferometry controls the fundamental comb offset frequency f_0 . **c**, fsEC design consisting of four gold mirrors and a 500- μm -thick, 1° -wedged diamond plate. **d**, Schematic of the near-IR (blue) and mid-IR (MIR; red) comb modes versus cavity resonances (grey). The HC lock controls f_{rep} to overlap the cavity resonances and the near-IR comb modes (right; passing a 12-nm-wide, 1,550-nm-centre-wavelength bandpass filter), fixing the relative position of the mid-IR resonances and offset-free comb modes (left) in the frequency space. Tuning f_0 , thus, results in a linear change in f_{rep} , bringing the mid-IR comb lines into resonance with fsEC. **e**, Intensity at the fsEC transmission port for near-IR (blue) and mid-IR (red) and HC error signal (cyan) as a function of f_{rep} .

use of unprotected gold-coated mirrors. It, furthermore, avoids etalon effects caused by spatially overlapping multiple reflections in a parallel-plate IC²⁹. In the following, the terms reflection port and transmission port are used in relation to the fsEC (Fig. 1c) to describe the physical effects at the respective ports. This nomenclature is consistent with the fsEC literature, which mostly uses transmission through one of the cavity mirrors for input coupling (Fig. 1a). In our coupling scheme, the beam transmitted through the IC instead of the one reflected off the IC interferes with the pulses coupled out of the cavity. Input coupling takes place at the upper interface of the wedge (Fig. 1a, inset), whereas the lower interface takes on the role of an output coupler.

Figure 1d demonstrates how locking the fundamental near-IR comb to the cavity creates a linear link between the independent degrees of freedom f_{rep} and f_0 of the oscillator. Adjusting f_0 , maintaining the lock in the near-IR regime, and recording the spectra transmitted through the fsEC allowed for scanning over the resonances and thus gaining information about finesse and dispersion of the fsEC (Fig. 2). The gold and diamond optics exhibit low dispersion across a broad bandwidth, allowing for the simultaneous enhancement of more than three octaves, provided that the

seeding comb modes can be overlapped with the cavity resonances by tuning both f_{rep} and f_0 (Fig. 2a, left). Our IPDFG comb, however, has zero offset frequency, which inherently cannot match the optimum offset frequency (OOF)³⁰ required by the empty cavity (Methods). We overcome this obstacle by filling the cavity with a gas (here humidity-controlled air) and thus shifting the fsEC's OOF and introducing minimum dispersion in the 8–15 μm range. This procedure enables the enhancement of a nearly octave-spanning spectrum (theory, Fig. 2a (grey areas, right); experiment, Fig. 2b). For a proof-of-principle spectroscopic measurement, we additionally introduced 1 ppm methanol into the chamber as an IR-active molecular sample.

We characterized the fsEC by recording the mid-IR spectra using a commercial FTIR spectrometer at the fsEC transmission port as f_0 is tuned (Methods). Figure 2b shows the power spectral density (PSD) enhancement as a function of the resulting change in f_{rep} , determined from these data. The simultaneous enhancement over the 22–40 THz band agrees well with the numerical model (the red dashed line tracks the position of maximum enhancement; Methods). The fsEC finesse was also obtained from the measured spectra and is depicted together with matching theoretical

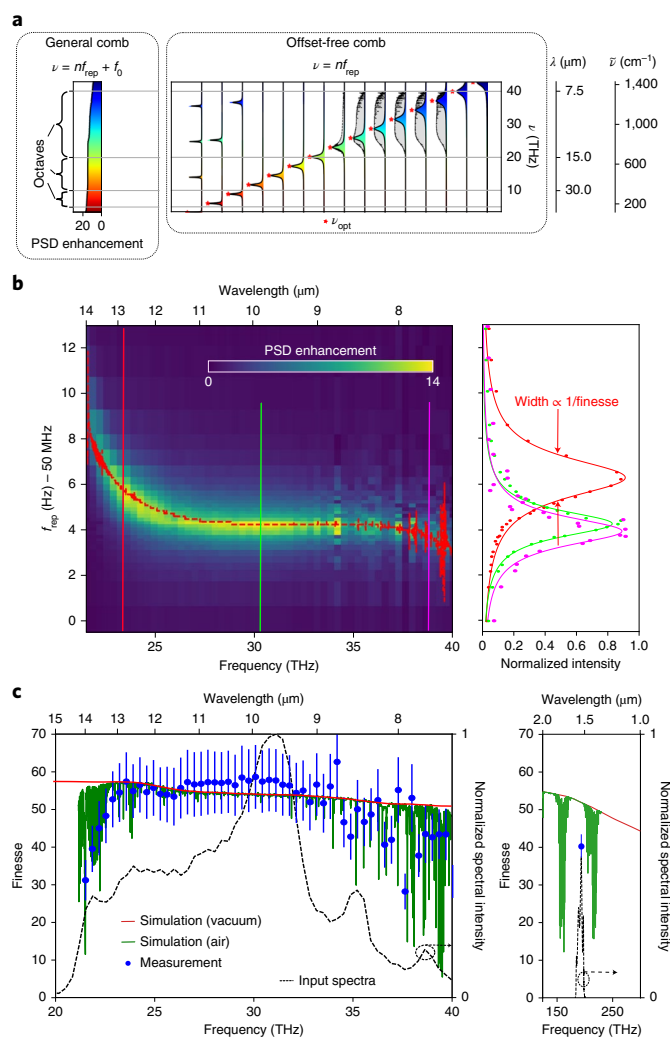


Fig. 2 | Characterization of fsEC in the mid-IR spectral region.

a, Theoretically achievable simultaneous multi-octave enhancement of the empty resonator when seeded with a two-parameter-tunable frequency comb (left). Theoretically achievable multi-octave-tunable enhancement for an offset-free comb (solid lines) (right). Different optical frequencies ν_{opt} (star-shaped markers) are enhanced by tuning the comb repetition rate f_{rep} . Adjusting dispersion by means of a humidity-controlled air background allows for simultaneous enhancement of almost an octave (dashed lines). **b**, Measured spectrally resolved enhancement as a function of repetition rate when operating with an offset-free mid-IR comb and the chamber filled with humidity-controlled air (left). The data are derived from FTIR spectroscopy performed at the fsEC transmission port (Methods). The red dashed line (theory; corresponding to **a**) indicates the optimum-enhancement repetition rate for each mid-IR frequency and the vertical lines show the positions of the linecuts (right; normalized). **c**, Measured and theoretical fsEC finesse as a function of frequency for two spectral windows in the IR range. The blue dots represent the measured finesse, with error bars computed using the co-variance of the fit (using the dark-noise-signal standard deviation of the FTIR spectrometer as an estimate for the noise on the spectra) and Gaussian error propagation. The finesse at 200 THz was estimated from an oscilloscope trace of the narrowband comb swept over the fsEC resonances. The red line depicts the expected finesse for the empty resonator, and the green line for the resonator filled with humidity-controlled air (Methods). The input spectrum is represented as a black dashed line.

predictions for the empty and (humidity-controlled) air-filled chamber and the input spectra (Fig. 2c).

We analysed the waveforms reflected by the fsEC (with locking parameters enabling maximum enhancement) using EOS. They consist of the excitation pulse, followed by the much weaker molecular response (Fig. 3). The black line represents data recorded when the fsEC was tuned in the off-resonance condition (Fig. 3a, left inset). Owing to the high transmittivity of the IC, this beam corresponds to a single pass of almost the full seeding intensity through approximately 6.5 m of the gas-filled chamber. The red dataset (Fig. 3a, right inset) is measured with the comb locked to the ultrabroadband working point described above, and features a reduced maximum amplitude. This attenuation (Fig. 3b) is due to the destructive interference between the output-coupled intracavity beam and the portion of the seed transmitted through the IC (Fig. 1a). Due to the imperfect transverse mode and impedance matching, the reduction in amplitude in the main pulse amounts to only 38%, which, nevertheless, corresponds to an intensity suppression of more than 60%. The molecular response generated inside the fsEC leaks out without destructive interference (Fig. 3c). The improved ratio between the long-lasting oscillations rich in spectroscopic information and the comparatively strong excitation benefits power scaling and relaxes the demands on the dynamic range of the detection scheme. Note that interferometric suppression of the excitation profits both time-resolved spectroscopy where it adds to the advantages of temporal filtering and time-integrating detection schemes.

Further analysis of these traces was performed in the frequency domain. Figure 4a shows the amplitude spectra corresponding to a single pass through the chamber (path length, 6.5 m; black) and to pulses recorded in the on-resonance condition (red). The latter is interference between the single pass and output-coupled portion of the circulating field. The availability of amplitude and phase information through EOS detection readily allows for the reconstruction of the intracavity pulses by forming the difference between the single-pass and on-resonance signals (blue). The numerical prediction for the intracavity spectrum is depicted as a dashed grey line, and the discrepancy between theory and experiment is attributed to imperfect mode matching (Methods). The spectrum of the single-pass EOS signal (Fig. 4a, inset) shows only weak resonant features connected to molecular vibrations. The on-resonance signals, on the other hand, feature these narrowband resonances stronger due to the increased effective path length. Sampling the electric field in the time domain enables the temporal filtering of the recorded signals, isolating molecular emission from the excitation¹⁶ (Fig. 4b). This step reveals a plethora of emission peaks at frequencies coinciding with the HITRAN database³¹ absorption data for water (14% humidity), CO₂ (360 ppm) and methanol (1 ppm), as expected from the calculations (Methods). The dominant peak from the molecular re-emission of methanol close to 30 THz is enhanced by a factor of 6 compared with the single-pass data. This value is compatible with PSD enhancement (Fig. 2), taking into account the imperfect transverse-mode matching (estimated to be 40%; Methods).

In conclusion, we have demonstrated the passive enhancement of nearly octave-spanning, waveform-stable few-cycle mid-IR pulses in a low-dispersion fsEC, and quantitative cavity-enhanced field-resolved vibrational spectroscopy of gases. Our setup features, to the best of our knowledge, the broadest simultaneously enhanced frequency comb demonstrated so far, as well as the first fsEC for a frequency comb covering wavelengths beyond 4 μm , including the difficult-to-access region above 10 μm .

The enhancement of waveform-stable pulses permitted the detection of optical waveforms carrying a cavity-enhanced molecular response via EOS for the first time. We directly observed the time-dependent interference at the IC, showing an improvement of

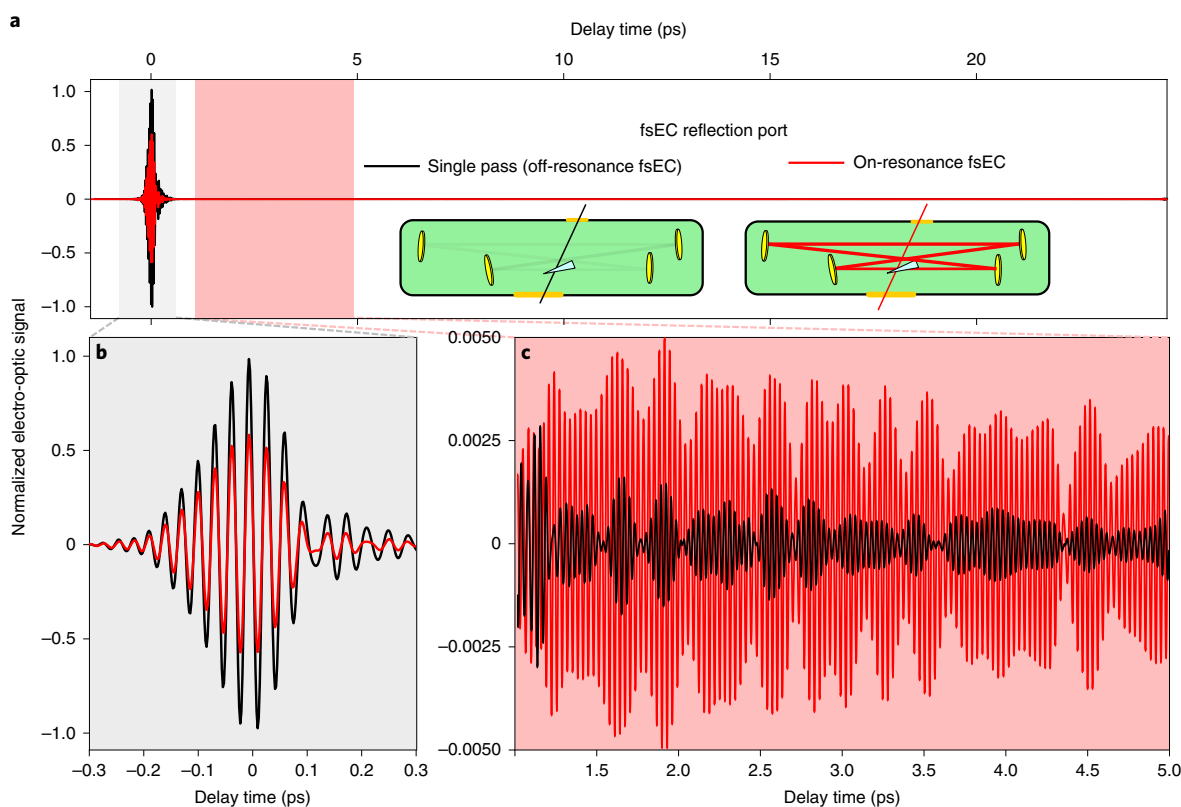


Fig. 3 | EOS signals recorded at the fsEC reflection port. **a**, Scan showing the excitation pulse and molecular response. The inset displays the two different beam paths generating the traces. The black line indicates the EOS scan corresponding to a single pass (fsEC in the off-resonance condition) through the gas-filled chamber with a path length close to one round trip of the fsEC. The red line indicates the EOS scan of the beam reflected off the fsEC locked on resonance (interference of the transmission through the IC and intracavity radiation coupled out). **b**, Magnified representation of the excitation pulse. The destructive interference of the input beam with the intracavity light in this direction leads to a reduced amplitude of the waveform when the mid-IR comb is locked to the fsEC. **c**, Magnified region in the wake of the excitation pulse, predominantly containing the re-emitted molecular response, which is enhanced by the resonant cavity compared with the single pass. The time-domain data were bandpass filtered with a bandwidth of 10 THz around a centre frequency of 30.5 THz.

the contrast between the cavity-enhanced molecular response and the ultrashort excitation reflected by the fsEC. This effect relaxes the dynamic range requirements for linear detection via EOS and potentially grants access to the leading higher-amplitude part of the molecular response to an ultrashort excitation in the presence of excessive excitation intensity noise¹⁶. Combined with recent improvements in EOS sensitivity in the mid-IR spectral region^{32,33}, broadband spectroscopy of mixed gaseous samples with detection limits in the lower parts-per-trillion range (Methods) come into reach.

This extension of fsEC technology, providing optical-field enhancement of few-cycle pulses at high repetition rates, to the long-wave mid-IR range promises novel applications. These include—but are not limited to—the high-precision investigation of nonlinear light–matter interactions, aided by the tunable CEP, and their exploitation for frequency conversion as well as the exploration of low-energy excitations in non-equilibrium condensed-matter systems^{34,35}.

Online content

Any methods, additional references, Nature Research reporting summaries, source data, extended data, supplementary information, acknowledgements, peer review information; details of author contributions and competing interests; and statements of data and code availability are available at <https://doi.org/10.1038/s41566-022-01057-0>.

Received: 9 November 2021; Accepted: 7 July 2022;

Published online: 22 August 2022

References

- Jones, R. J. & Ye, J. Femtosecond pulse amplification by coherent addition in a passive optical cavity. *Opt. Lett.* **27**, 1848–1850 (2002).
- Gagliardi, G. & Loock, H.-P. (eds) *Cavity-Enhanced Spectroscopy and Sensing* (Springer, 2014).
- Adler, E., Thorpe, M. J., Cossel, K. C. & Ye, J. Cavity-enhanced direct frequency comb spectroscopy: technology and applications. *Annu. Rev. Anal. Chem.* **3**, 175–205 (2010).
- Lisak, D. et al. Dual-comb cavity ring-down spectroscopy. *Sci Rep.* **12**, 2377 (2022).
- Reber, M. A. R., Chen, Y. & Allison, T. K. Cavity-enhanced ultrafast spectroscopy: ultrafast meets ultrasensitive. *Optica* **3**, 311–317 (2016).
- Allison, T. K. Cavity-enhanced ultrafast two-dimensional spectroscopy using higher order modes. *J. Phys. B* **50**, 044004 (2017).
- Peters, E. et al. A deep-UV optical frequency comb at 205 nm. *Opt. Express* **17**, 9183–9190 (2009).
- Gohle, C. et al. A frequency comb in the extreme ultraviolet. *Nature* **436**, 234–237 (2005).
- Jones, R. J., Moll, K. D., Thorpe, M. J. & Ye, J. Phase-coherent frequency combs in the vacuum ultraviolet via high-harmonic generation inside a femtosecond enhancement cavity. *Phys. Rev. Lett.* **94**, 193201 (2005).
- Pupez, I., Zhang, C., Högnér, M. & Ye, J. Extreme-ultraviolet frequency combs for precision metrology and attosecond science. *Nat. Photon.* **15**, 175–186 (2021).
- Todd, M. W. et al. Application of mid-infrared cavity-ringdown spectroscopy to trace explosives vapor detection using a broadly tunable (6–8 μm) optical parametric oscillator. *Appl. Phys. B* **75**, 367–376 (2002).

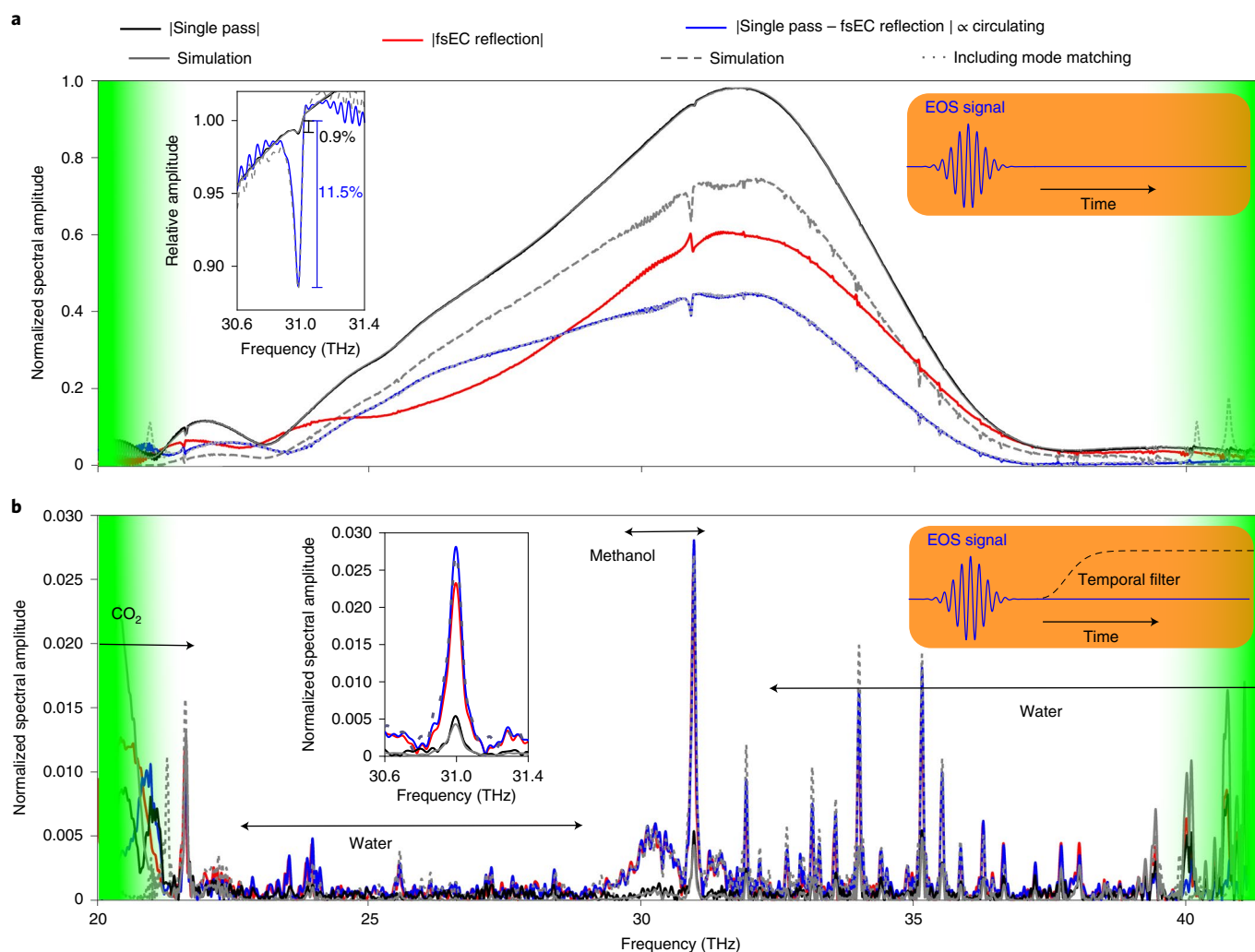


Fig. 4 | Spectra of EOS traces measured at the fsEC reflection port. a, Spectral amplitudes computed from the EOS traces of the excitation pulse and molecular response (sketch). The red line indicates the reflection off the fsEC with the seeding comb locked to a setting that enables the maximum power enhancement around 30 THz. The black line indicates propagation through the gas-filled chamber and cavity IC with the fsEC in the off-resonance condition (solid grey, corresponding simulation). The blue line indicates the difference between the single pass and fsEC reflection, which is proportional to the circulating spectrum (dashed grey, corresponding simulation assuming perfect mode matching; dotted grey, simulation accounting for the mode-matching factor; Methods). The green areas mark the spectral region in which the fsEC enhancement vanishes (due to water-vapour and CO₂ resonances). The inset shows the data normalized to the expected spectral amplitude at 31 THz assuming negligible absorption by methanol and illustrates the 12-fold increase in the relative dip depth (unaffected by imperfect mode matching), in agreement with the numerical model (dashed lines). **b**, Spectral amplitudes of the EOS traces with the excitation removed by a soft window (sketch in inset and Methods), showing a sixfold improvement owing to limited mode matching. The grey lines indicate numerical predictions for both single pass (solid) and circulating (dotted; includes mode matching) molecular re-emissions (Methods). The acquisition time of the measurements is 40 s and the frequency resolution is 2.5 GHz.

12. Snee, M., Hannemann, S., van Duijn, E. J. & Ubachs, W. Deep-ultraviolet cavity ringdown spectroscopy. *Opt. Lett.* **29**, 1378–1380 (2004).
13. Foltynowicz, A., Ban, T., Masłowski, P., Adler, F. & Ye, J. Quantum-noise-limited optical frequency comb spectroscopy. *Phys. Rev. Lett.* **107**, 233002 (2011).
14. Bernhardt, B. et al. Vacuum ultraviolet frequency combs generated by a femtosecond enhancement cavity in the visible. *Opt. Lett.* **37**, 503–505 (2012).
15. Lilienfein, N. et al. Enhancement cavities for few-cycle pulses. *Opt. Lett.* **42**, 271–274 (2017).
16. Pupeza, I. et al. Field-resolved infrared spectroscopy of biological systems. *Nature* **577**, 52–59 (2020).
17. Ye, J., Ma, L.-S. & Hall, J. L. Ultrasensitive detections in atomic and molecular physics: demonstration in molecular overtone spectroscopy. *J. Opt. Soc. Am. B* **15**, 6–15 (1998).
18. Gohle, C., Stein, B., Schliesser, A., Udem, T. & Hänsch, T. W. Frequency comb Vernier spectroscopy for broadband, high-resolution, high-sensitivity absorption and dispersion spectra. *Phys. Rev. Lett.* **99**, 263902 (2007).
19. Silfies, M. C. et al. Widely tunable cavity-enhanced frequency combs. *Opt. Lett.* **45**, 2123–2126 (2020).
20. Foltynowicz, A., Masłowski, P., Fleisher, A. J., Bjork, B. J. & Ye, J. Cavity-enhanced optical frequency comb spectroscopy in the mid-infrared application to trace detection of hydrogen peroxide. *Appl. Phys. B* **110**, 163–175 (2013).
21. Consolino, L. et al. Bow-tie cavity for terahertz radiation. *Photonics* **6**, 1 (2018).
22. Winkler, G. et al. Mid-infrared interference coatings with excess optical loss below 10 ppm. *Optica* **8**, 686–696 (2021).
23. Catanese, A. et al. Mid-infrared frequency comb with 6.7 W average power based on difference frequency generation. *Opt. Lett.* **45**, 1248–1251 (2020).
24. Torgerson, J. & Nagourney, W. Tunable cavity coupling scheme using a wedged plate. *Opt. Commun.* **161**, 264–266 (1999).
25. Ru, Q. et al. Self-referenced octave-wide subharmonic GaP optical parametric oscillator centered at 3 μ m and pumped by an Er-fiber laser. *Opt. Lett.* **42**, 4756–4759 (2017).

26. Wu, Q. & Zhang, X. -C. Free-space electro-optic sampling of terahertz beams. *Appl. Phys. Lett.* **67**, 3523 (1995).
27. Kübler, C., Huber, R., Tübel, S. & Leitenstorfer, A. Ultrabroadband detection of multi-terahertz field transients with GaSe electro-optic sensors: approaching the near infrared. *Appl. Phys. Lett.* **85**, 3360 (2004).
28. Kowligy, A. S. et al. Infrared electric field sampled frequency comb spectroscopy. *Sci. Adv.* **5**, eaaw8794 (2019).
29. Lykke, K. R. Internally-coupled build-up cavity for frequency doubling of cw lasers. *Opt. Commun.* **157**, 88–92 (1998).
30. Holzberger, S. et al. Enhancement cavities for zero-offset-frequency pulse trains. *Opt. Lett.* **40**, 2165–2168 (2015).
31. Gordon, I. E. et al. The HITRAN2016 molecular spectroscopic database. *J. Quant. Spectrosc. Radiat. Transf.* **203**, 3–69 (2017).
32. Riek, C. et al. Direct sampling of electric-field vacuum fluctuations. *Science* **350**, 420–423 (2015).
33. Hofer, C. et al. Mid-infrared electric field sampling approaching single-photon sensitivity. *EPJ Web Conf.* **243**, 16001 (2020).
34. Schubert, O. et al. Sub-cycle control of terahertz high-harmonic generation by dynamical bloch oscillations. *Nat. Photon.* **8**, 119–123 (2014).
35. Lomsadze, B. & Cundiff, S. T. Frequency combs enable rapid and high-resolution multidimensional coherent spectroscopy. *Science* **357**, 1389–1391 (2017).

Publisher's note Springer Nature remains neutral with regard to jurisdictional claims in published maps and institutional affiliations.



Open Access This article is licensed under a Creative Commons Attribution 4.0 International License, which permits use, sharing, adaptation, distribution and reproduction in any medium or format, as long as you give appropriate credit to the original author(s) and the source, provide a link to the Creative Commons license, and indicate if changes were made. The images or other third party material in this article are included in the article's Creative Commons license, unless indicated otherwise in a credit line to the material. If material is not included in the article's Creative Commons license and your intended use is not permitted by statutory regulation or exceeds the permitted use, you will need to obtain permission directly from the copyright holder. To view a copy of this license, visit <http://creativecommons.org/licenses/by/4.0/>.

© The Author(s) 2022

Methods

The laser system including mid-IR generation and EOS is based on a commercial Er:fibre frequency comb (Menlo C-Fiber; $f_{\text{rep}} = 100$ MHz). Pulse picking reduces f_{rep} to 50 MHz and a nonlinear Raman fibre shifts its spectrum to a wavelength of 1,965 nm. Employing these seeding pulses, a chirped-pulse-amplification system with two Tm:fibre amplifiers yields an output power of up to 40 W at a pulse duration of 250 fs. In two separate branches, photonic crystal fibres are employed for nonlinear self-compression at a centre wavelength of 2 μm (ref. 36). The 30 fs output drives the IPDFG and the 13 fs output is used for temporal gating in EOS. For EOS, the mid-IR pulses from the fsEC reflection port are spatially and temporally overlapped with the near-IR gate pulses in a 541- μm -thick GaSe crystal. The second-order nonlinearity of this crystal maps the electric field of the mid-IR pulses into a polarization change of the near-IR beam. The electro-optic signal is recorded using balanced detection and by scanning the gate-pulse delay with a mechanical stage³⁶.

Locking the Er:fibre comb to fsEC. The polarization discrimination introduced by the wedged IC lends itself to the implementation of the Hänsch–Couillaud locking scheme³⁷. Its error signal acts on the fundamental frequency comb's repetition rate via actuators provided by the manufacturer. The seeding frequency comb system also provides independent control over f_0 .

Parameters of empty fsEC. The 6-m-long fsEC (Fig. 1c) comprises two plane mirrors, two 1,000-mm-radius-of-curvature spherical mirrors placed 1,064 mm apart and wedged-diamond IC (wedge angle, 1°; thickness, 300 μm). The mid-IR seeding beam impinges on the IC at an angle of incidence (56.8°) offset from Brewster's angle (67.2°), with a measured reflectivity of $R_{\text{IC}} = 4.3\%$ (Fig. 1c, inset). After traversing the fsEC, the beam is reflected at the first surface of the IC into the fsEC transmission port ($R_{\text{OC},t} = 2.7\%$) and at the second surface into the fsEC reflection port ($R_{\text{OC},r} = 4.0\%$). Absorption (0.7%) and Fresnel ($R_{\text{OC},t} + R_{\text{OC},r}$) losses in the diamond wedge and 1.0% loss at each gold mirror amount to a total round-trip loss of the empty fsEC of 11.0% (that is, the round-trip transmission is $T_{\text{cav}} = 1.0 - 11.0\% = 89.0\%$). The round-trip phase ϕ_{cav} comprises the geometrical phase ('OOF' section), phase on reflection from the gold mirrors (180°), and phase from the Fresnel transmission coefficients on the diamond-wedge interfaces and transmission through the diamond material. The transmission of the seed through the wedge, directly to the fsEC reflection port, is $T_{s,r} = 90.1\%$. The group-delay dispersion of the IC in transmission is less than 6 fs². Thus, the refraction angle of the wedge differs by 17 μrad between the spectral components at 20 and 40 THz, causing a deviation between the optical axes of the eigenmode at these frequencies by less than 0.1% of the centre-frequency beam diameter, over the entire fsEC beam path (calculated with the 3 \times 3 ray transfer matrix formalism³⁸). Brewster's angle and Fresnel coefficients were obtained from (real) refractive index (1.0–100.0 μm) and absorption (2.5–15.0 μm) data of the diamond IC, provided by the manufacturer (Diamond Materials). Diamond was chosen as the material because of its large electronic bandgap (corresponding to an ultraviolet wavelength) and because its non-polarity and symmetry prohibit single-phonon excitation by IR radiation. The remaining absorption due to impurities and higher-order processes (most importantly, multiphonon absorption between 2.5 and 6.0 μm) are known to depend on growth conditions. We use manufacturer data and neglect absorption where unavailable (>15.0 μm and between 1.0 and 2.5 μm). The reflection coefficient of the gold mirrors (including the phase) was calculated from its complex refractive index³⁹. All the fsEC optics are hit with light polarized in the plane of incidence. The weak spectral dependency of the figures stated here is fully accounted for in the numerical model. The given values are (to the provided number of digits) valid in the 20–40 THz range.

OOF. Because the seeding comb obtained by IPDFG is intrinsically offset free, the fsEC must be engineered for an OOF of zero to enable simultaneous broadband enhancement. The OOF is determined by the round-trip spectral phase of the resonator, which has contributions from the optics itself and the geometrical phases acquired during propagation. Our optics have negligible dispersion ('Parameters of empty fsEC' section) and only a very small CEP shift (four gold-coated mirrors without a protective layer, -0.2° ; 300- μm -thick diamond, 2.5° ; determined for the measured seed spectrum described above). The total round-trip CEP shift is, therefore, nearly exclusively determined by the geometrical (Gouy) phases $\psi = (n + m + 1) \sum_i (\arg q_{\text{end},i}^{-1} - \arg q_{\text{start},i}^{-1})$, where n and m are the transverse-mode numbers of the excited Hermite–Gaussian cavity eigenmode, and $q_{\text{start},i}$ and $q_{\text{end},i}$ are the complex beam parameters after the first and before the second optical element for the i th free-space propagation inside the resonator, respectively. However, a resonator with a vanishing total geometrical phase and optical elements that do not induce a CEP shift is inherently unstable for the fundamental transverse mode: due to the $(n + m + 1)$ prefactor, the geometrical phase equals to zero for all the transverse modes, that is, all the modes would be simultaneously resonant. For a bowtie cavity, it is well known that this situation is only possible at the resonator's stability edges⁴⁰. To address this problem, the resonator can, in principle, be operated with a higher-order transverse mode (at the expense of achievable enhancement due to the reduced spatial overlap with the

seed), or an additional optical element with a larger CEP shift can be introduced (in general, at the expense of a decrease in bandwidth due to increased dispersion). Here we chose the latter option, and filled the chamber with humid air (CEP shift of 132.2° for 14% humidity and 360 ppm CO₂) to permit a round-trip CEP shift of zero and broadband operation in a stable resonator with the fundamental Hermite–Gaussian transverse eigenmode. The humidity was controlled by filling the chamber with nitrogen and mixing in humid air until broadband operation was achieved. The relative humidity was measured with a consumer-electronics sensor ($16.0 \pm 3.8\%$) and was found to be in line with the value expected from the numerical model (14.0%).

Model of fsEC. Figure 2a shows the PSD enhancement

$$\varepsilon(\nu) = \left| \frac{\sqrt{R_{\text{IC}}(\nu)}}{1 - \sqrt{T_{\text{cav}}(\nu)} e^{i\phi_{\text{cav}}(\nu) - i(2\pi\nu t_{\text{rep}} + \Delta\phi)}} \right|^2 \quad \text{for an fsEC with an input coupling ratio}$$

$R_{\text{IC}}(\nu)$, round-trip transmission $T_{\text{cav}}(\nu)$ (including Fresnel and absorption losses on the IC), round-trip phase $\phi_{\text{cav}}(\nu)$, seeding-pulse-train repetition period t_{rep} and CEP slippage $\Delta\phi$. The values for $R_{\text{IC}}(\nu)$, $T_{\text{cav}}(\nu)$ and $\phi_{\text{cav}}(\nu)$ were obtained as described in the 'Parameters of empty fsEC' section. For $T_{\text{cav}}(\nu)$ and $\phi_{\text{cav}}(\nu)$, we additionally considered the humid-air complex refractive index, assembled from the complex line profiles with Lorentz parameters from HITRAN^{31,41}, for water vapour (14% relative humidity), CO₂ (360.0 ppm) and CH₄ (1.8 ppm) at standard temperature and pressure, as well as the Gouy phase shifts for the GH₀₀ eigenmode (determined by the fsEC geometry; 'Parameters of empty fsEC' section). Water-vapour and CO₂ concentrations were chosen for best agreement with the experimental data. The pulse-train parameters t_{rep} and $\Delta\phi$ are related to the comb parameters f_0 and f_{rep} and were optimized for best enhancement around the optical frequencies marked with the red star symbols in Fig. 2a. The PSD enhancement $\varepsilon(\nu)$ for $f_0 = \Delta\phi = 0$ was computed versus ν and f_{rep} and the position of maximum enhancement for each value of ν was determined and depicted as a red line for comparison with the experimental data (Fig. 2b). Figure 2c shows the simulated finesse: $F(\nu) = \frac{\pi}{1 - \sqrt{T_{\text{cav}}(\nu)}}$. Both datasets were calculated with a frequency resolution of 342 MHz.

Finesse and PSD enhancement measurement. The PSD at the fsEC transmission port, $S_{\text{trans}}(\nu, f_0)$, was measured using an FTIR spectrometer while the near-IR fundamental comb was locked to the cavity and its f_0 was tuned, leading to a change in f_{rep} of both fundamental near-IR and mid-IR combs. The repetition rate relates to f_0 (measured with f -2f interferometry) via the comb equation $\nu_{\text{NIR}} = 193 \text{ THz} = n f_{\text{rep}} + f_0$, where $f_0 \ll n f_{\text{rep}}$ and thus $n \approx \nu_{\text{NIR}}/f_{\text{rep}} = 1.9 \times 10^6$. Consequently, a change in f_0 causes a change in repetition rate $\Delta f_{\text{rep}} \approx \Delta f_0/n$. In turn, the repetition rate f_{rep} is associated with the frequency of the mid-IR comb modes $\nu = m(f_{\text{rep}}/2)$, where m is the mode number and $f_{\text{rep}}/2$ is the repetition rate after pulse picking.

To obtain the finesse, slices of $S_{\text{trans}}(\nu, f_0)$ for each ν are plotted versus $\Delta\nu = (1/2)m\Delta f_{\text{rep}} = (1/2)\nu/(f_{\text{rep}}/2)\Delta f_0/n$. A Lorentzian function was then fitted to the linecuts and the free spectral range (50 MHz) of the fsEC was divided by the full linewidth evaluated at half maximum, yielding the frequency-dependent finesse $F(\nu)$ (Fig. 2c; examples for the line shapes are shown in Fig. 2b, right).

From the finesse, we first calculated the on-resonance PSD enhancement for each ν :

$$\varepsilon_{\text{res}}(\nu) = \left| \frac{\sqrt{R_{\text{IC}}}}{1 - \sqrt{T_{\text{cav}}(\nu)}} \right|^2 = \frac{F^2(\nu)}{\pi^2} R_{\text{IC}}.$$

The PSD enhancement (Fig. 2b) was then obtained as

$$\begin{aligned} \varepsilon(\nu, \Delta f_{\text{rep}}) &= \varepsilon(\nu, \Delta f_{\text{rep}}) \times \frac{\varepsilon_{\text{res}}(\nu, \Delta f_{\text{rep}})}{\max_{\nu} \varepsilon(\nu, \Delta f_{\text{rep}})} \\ &= S_{\text{trans}}(\nu, n\Delta f_{\text{rep}}) \times \frac{\varepsilon_{\text{res}}(\nu, \Delta f_{\text{rep}})}{\max_{\nu} S_{\text{trans}}(\nu, n\Delta f_{\text{rep}})}, \end{aligned}$$

where we have used $S_{\text{trans}}(\nu, f_0) \propto \varepsilon(\nu, \Delta f_{\text{rep}})$ with the proportionality constant $S_{\text{in}}(\nu)O(\nu)R_{\text{OC},t}$. Here $S_{\text{in}}(\nu)$ denotes the seed PSD, $O(\nu)$ is the spatial overlap and $R_{\text{OC},t}$ is the output-coupling ratio via the fsEC transmission port. Similar methods to characterize an fsEC with just one frequency comb are presented elsewhere^{42,43}.

Because the optical-frequency resolution of the FTIR spectrometer measurements (0.14 THz) was not sufficient to resolve the much narrower absorption lines of the intracavity gas, the accuracy of this method is poor in regions with strong absorption lines. Spectral averaging then leads to an apparent broadening (due to vertical deflection; Fig. 2b, red dashed line) of the Lorentzian and thus to a small deviation from the frequency-bin-averaged finesse and PSD enhancement. To quantify this effect, we have synthesized the high-frequency-resolution (342 MHz) $S_{\text{trans}}(\nu, f_0)$ data with the numerical model (including gas dispersion and absorption), reduced it to the experimental ν and f_0 bins by averaging, and applied the same evaluation as the experimental data. In the spectral region of 23–37 THz, we have found at most 3% deviation of the evaluated finesse from the actual finesse averaged to the same resolution. In the vicinity

of the strong molecular absorptions due to water vapour and CO₂ (20–23 and 37–40 THz), we found an underestimation, by at most 15%.

Path-length enhancement. The path-length enhancement η relates to the PSD enhancement ε and input/output coupling ratios of the fsEC as follows: for an absorber in the cavity, the on-resonance field enhancement is $\sqrt{\varepsilon\alpha} = \frac{\sqrt{R_{IC}}}{1 - \sqrt{T_{cav}}e^{-\alpha l/2}}$ (ν dependence is omitted for clarity; cavity length l ; attenuation coefficient α). The total cavity transmission coefficient is obtained as the product of field enhancement $\sqrt{\varepsilon\alpha}$ and output-coupler transmission coefficient $\sqrt{R_{OC}}$: $H_{total} = \sqrt{\varepsilon\alpha}\sqrt{R_{OC}}$. For small α , $\partial_\alpha H_{total} \approx -l/2H_{total}F/\pi\sqrt{T_{cav}}$. Comparing with the corresponding single-pass value $\partial_\alpha H_{sp} \approx -l/2$ yields the path-length enhancement due to an absorber, that is, $\eta = \partial_\alpha H_{total}/\partial_\alpha H_{sp} = H_{total}F/\pi\sqrt{T_{cav}} \approx H_{total}F/\pi$. For a lossless cavity, $H_{total} \approx 1$, which yields the well-known formula F/π (for a travelling-wave cavity as in our case; for a standing-wave cavity, it is $2F/\pi$ ⁴⁴). In our case, a substantial part of the seeding energy is dissipated in the cavity optics ('Parameters of empty fsEC' section) such that here the general formula for amplitude-change enhancement has to be invoked: $\eta \approx H_{total} \frac{F}{\pi} = \sqrt{\varepsilon}\sqrt{R_{OC}}\sqrt{\varepsilon}/\sqrt{R_{IC}} = \varepsilon\sqrt{R_{OC}/R_{IC}}$. For $\varepsilon = 13.6$ (measured in the on-resonance condition at 30 THz; Fig. 2b), the expected path-length enhancement for detection via the fsEC reflection port ($R_{OC} = R_{OC,r} = 4\%$) is 13.1. Detection via the fsEC transmission port ($R_{OC} = R_{OC,t} = 2.7\%$) would yield a slightly lower path-length enhancement of 10.8 instead of 13.1.

With 40% transverse-mode overlap ('Mode matching' section), the expected PSD enhancement and thus the path-length enhancement reduces to $13.1 \times 40\% = 5.2$ (Fig. 4b). In the case of perfect mode matching (for example, spatially filtered seeding model; 'Mode matching' section) and impedance matching (for example, custom-manufactured diamond wedge where the transmission port surface is placed under Brewster's angle), a cavity with four gold mirrors (loss, 1%; $1 - T_{cav} = 2R_{IC} = 2 \times 4\%$) would permit power and path-length enhancement of 24. For the case of lossless mirrors, the 0.7% internal losses in the diamond-wedge IC would be the limiting factor for the path-length enhancement, yielding a value of 143.

Suitability of fsEC for ultrashort pulses. The circulating pulses in the cavity are subject to the dispersion of the fsEC transfer function (f_{rep} chosen for the maximum bandwidth). On resonance, the FTIR spectrum measured at the fsEC transmission port ('Finesse and PSD enhancement measurement' section) supports a Fourier limit of 53 fs (1.6 cycles at a carrier frequency of 31 THz). To estimate the effect of fsEC dispersion on pulse duration, we apply the spectral phase of the transfer function to the Fourier-limited spectrum, obtaining a slightly elongated 55 fs pulse.

Evaluation and simulation of EOS traces. To reproduce the single-pass spectrum with the numerical model (Fig. 4, grey line), the excitation of the measured single-pass EOS trace was isolated with a temporal filter (piecewise cos² window, 0-to-1 rise interval from -0.7 to -0.6 ps, 1-to-0 drop interval from 0.9 to 1.0 ps relative to the maximum of the trace). In the frequency domain, this operation results in a smooth version of the single-pass spectrum (without dips due to molecular absorption). Propagation of this estimate for the excitation through the fsEC chamber and EOS chamber is described by multiplication of the complex spectrum by $e^{-in_c \frac{2\pi\nu}{c} l_c}$ and $e^{-in_e \frac{2\pi\nu}{c} l_e}$, respectively, where n_c is the intracavity medium's complex refractive index, including 1 ppm methanol ('Model of fsEC' section), and n_e is that for the EOS chamber (35% relative humidity of the ambient air, same CO₂ and CH₄ concentration, and no methanol). The path lengths in the fsEC chamber and EOS chamber are $l_c = 6.5$ m and $l_e = 1.0$ m, respectively. The resulting complex spectrum was then transformed back to the time domain, and the excitation was removed with the same soft window as used for the experimental data (cos² window with a 0-to-1 rise interval from 1.5 to 7.7 ps; Fig. 4b, inset). Figure 4b shows the agreement of the complex spectrum of the resulting trace with its measured counterpart. It must be stressed that the peaks in the simulated spectrum cannot be a remainder from the underlying single-pass EOS trace, because the two applied temporal filters (isolating the excitation and removing the molecular re-emission) are mutually exclusive. The EOS signal was recorded at the fsEC reflection port and the fsEC detuned from resonance is a good approximation for a single pass through the chamber because most of the seeding power is transmitted through the IC; inside the cavity, the pulses do not interfere constructively.

Likewise, we obtain the simulated complex spectra corresponding to the output-coupled circulating pulses (Fig. 4a, dashed grey line) as follows: we multiplied the excitation's complex spectrum by the complex transmissions through the fsEC and EOS chambers (as mentioned above), on-resonance fsEC coupling coefficient ($\sqrt{R_{OC,r}}$), and we corrected for the wedge transmission coefficient included in the single-pass pathway ($1/\sqrt{T_{s,r}}$). Figure 4a shows the agreement of the relative dip depths of the simulated versus measured spectra (inset). The ratio of the relative dip depths for enhanced and single-pass methanol signal is $11.5\%/0.9\% = 12.8$, compared with an expected value of

$(l_e + \eta \times 6 \text{ m})/l_c = 13.1$, where $\eta = 13.1$ is the path-length enhancement ('Path-length enhancement' section).

Mode matching. The amplitude of the experimentally determined spectrum of the circulating pulses is smaller than the prediction from the numerical model, despite the fact that the measured and simulated finesse, as well as the derived PSD enhancement factor of the fsEC, agree well (Fig. 2). This discrepancy stems from the limited spatial overlap between the seeding transverse mode and cavity eigenmode, as well as the overlap between the beam from the fsEC reflection port and beam of EOS gating pulses. The ratio may be used to quantify the overall mode-matching factor combining seed pulses, fsEC and EOS detection. For this, we computed the squared ratio between the experimental and simulated intracavity complex spectrum (Fig. 4a). We obtained values between 35% and 70% in the 25–35 THz interval (40% at the position of the methanol feature, that is, 31 THz). In principle, the spatial overlap between the seed and fsEC may be increased further by filtering the seeding mode, for example, with a hollow-core single-mode mid-IR fibre⁴⁵, which would also improve the observed interferometric suppression of excitation. Figure 4b shows the agreement between the simulated output-coupled spectrum (dotted grey), corrected by the smoothed frequency-dependent mode-matching factor, and the measurement, after removing the excitation from both. We attribute the remaining discrepancies of the peak heights (1) to the approximation of the exciting pulses by temporal filtering as described above ('Evaluation and simulation of EOS traces' section) and (2) to the uncertainty in the CO₂ and water-vapour concentrations, which where—unlike methanol that was prepared with a standardized protocol suitable for low concentrations—not independently calibrated with sufficient precision, but chosen for best agreement with Fig. 2b. Finally, the error on the frequency-resolved enhancement contributes, too.

Limit of detection. The signal-to-noise ratio for the methanol peak at 31 THz (Fig. 4b) is approximately 50, suggesting that the limit of detection for the setup presented here (consisting of seed source, fsEC and detection via EOS) is 20 parts per billion. To estimate the achievable limit of detection for methanol under optimum use of our fsEC for path-length enhancement, we combine the assumptions of (1) an effective path length of 81 m, which is a property of our fsEC (and is independent of the source and detection) with (2) the ability to measure changes in the relative amplitude in a spectral element on the order of 10^{-6} , as recently demonstrated in the EOS of optical frequencies around 30 THz for an averaging time of 25 s and a 4.5 ps scanned time window¹⁶. At room temperature and 1 bar, the methanol absorption peak at 31 THz has an absorption coefficient^{31,41} of $\alpha = 21 \text{ cm}^{-1}$. With the assumptions ((1) and (2) above), this corresponds to an estimated detection limit of 12 parts per trillion (that is, a partial methanol pressure of $p = 12 \times 10^{-12} \text{ bar}$ at $l = 81 \text{ m}$ effective path length causes a relative spectral amplitude change of $\alpha l/2 \times \frac{p}{1 \text{ bar}} = 1/10^6$).

Data availability

The data and datasets that support the plots within this paper and other findings of this study are available from the corresponding authors upon reasonable request.

Code availability

The custom code used for the simulation of the cavity is available from the corresponding authors upon reasonable request.

References

- Butler, T. et al. Multi-octave spanning, Watt-level ultrafast mid-infrared source. *J. Phys. Photonics* **1**, 044006 (2019).
- Hänsch, T. W. & Couillaud, B. Laser frequency stabilization by polarization spectroscopy of a reflecting reference cavity. *Opt. Commun.* **35**, 441–444 (1980).
- Gerrard, A. & Burch, J. M. *Introduction to Matrix Methods in Optics* Appendix B (Dover Publications, 1975).
- Ordal, M. A., Bell, R. J., Alexander, R. W., Long, L. L. & Querry, M. R. Optical properties of Au, Ni, and Pb at submillimeter wavelengths. *Appl. Opt.* **26**, 744–752 (1987).
- Nagourney, W. *Quantum Electronics for Atomic Physics and Telecommunication* (Oxford Univ. Press, 2014).
- Kochanov, R. et al. HITRAN Application Programming Interface (HAPI): a comprehensive approach to working with spectroscopic data. *J. Quant. Spectrosc. Radiat. Transf.* **177**, 15–30 (2016).
- Thorpe, M. J., Jones, R. J., Moll, K. D., Ye, J. & Lalezari, R. Precise measurements of optical cavity dispersion and mirror coating properties via femtosecond combs. *Opt. Express* **13**, 882–888 (2005).
- Schliesser, A., Gohle, C., Udem, T. & Hänsch, T. W. Complete characterization of a broadband high-finesse cavity using an optical frequency comb. *Opt. Express* **14**, 5975–5983 (2006).

44. Romanini, D., Ventrillard, I., Méjean, G., Morville, J., & Kerstel, E. Intensity transmitted by a cavity: a simplified one-dimensional model. in *Cavity-Enhanced Spectroscopy and Sensing* (eds Gagliardi, G. & Loock, H. P.) (Springer, 2014).
45. Abel, T., Hirsch, J. & Harrington, J. A. Hollow glass waveguides for broadband infrared transmission. *Opt. Lett.* **19**, 1034–1036 (1994).

Acknowledgements

We thank F. Krausz and D. J. Jones for useful discussions. This research was undertaken thanks, in part, to funding from the Technology Transfer Program of the Max Planck Society (M.H.); the Max Planck-UBC-UTokyo Center for Quantum Materials (P.S. and M.H.); the Canada First Research Excellence Fund and Quantum Materials and Future Technologies Program (P.S.); the IMPRS-APS graduate school (D.G. and C.H.); the Max-Planck School of Photonics (D.G.); and the Research project 'SARSCoV2Dx' (13N15742), German Federal Ministry of Education and Research, within the funding program Photonics Research Germany (D.G.).

Author contributions

P.S., M.H. and I.P. designed and planned the experiments. P.S. coordinated the experiments. P.S., A.-K.R., L.F. and M.H. performed the experiments and analysed the

data. M.H. and A.-K.R. developed the model and performed the simulations. E.F. and L.V. contributed to the experimental concept. D.G. and C.H. provided and operated the amplifier system, mid-IR generation and EOS detection system. P.S., M.H., A.-K.R. and I.P. wrote the manuscript with input from all the other authors. I.P. supervised the project.

Funding

Open access funding provided by Max Planck Society.

Competing interests

The authors declare no competing interests.

Additional information

Correspondence and requests for materials should be addressed to Philipp Sulzer, Maximilian Högnér or Ioachim Pupeza.

Peer review information *Nature Photonics* thanks Piotr Masłowski and the other, anonymous, reviewer(s) for their contribution to the peer review of this work.

Reprints and permissions information is available at www.nature.com/reprints.